Notice

Crack to pulse transition and magnitude statistics during earthquake cycles on a self-similar rough fault

Elías Rafn Heimisson[a,*]

[a]*Seismological Laboratory, California Institute of Technology, Pasadena, California, USA*

Abstract

Faults in nature demonstrate fluctuations from planarity at most length scales that are relevant for earthquake dynamics. These fluctuations may influence all stages of the seismic cycle; earthquake nucleation, propagation, arrest, and inter-seismic behavior. Here I show quasi-dynamic plane-strain simulations of earthquake cycles on a self-similar and finite 10 km long rough fault with amplitude-to-wavelength ratio $\alpha = 0.01$. The minimum roughness wavelength, λ_{min}, and nucleation length scales are well resolved and much smaller than the fault length. Stress relaxation and fault loading is implemented using a variation of the backslip approach, which allows for efficient simulations of multiple cycles without stresses becoming unrealistically large. I explore varying λ_{min} for the same stochastically generated realization of a rough fractal fault. Decreasing λ_{min} causes the minimum and maximum earthquakes sizes to decrease. Thus the fault seismicity is characterized by smaller and more numerous earthquakes, on the other hand, increasing the λ_{min} results in fewer and larger events. However, in all cases, the inferred b-value is constant and the same as for a reference no-roughness simulation ($\alpha = 0$). I identify a new mechanism for generating pulse-like ruptures. Seismic events are initially crack-like, but at a critical length scale, they continue to propagate as pulses, locking in an approximately fixed amount of slip. I investigate this transition using simple arguments and derive a characteristic pulse length, $L_c = \lambda_{min}/(4\pi^4\alpha^2)$ and slip distance, δ_c based on roughness drag. I hypothesize that the ratio λ_{min}/α^2 can be roughly estimated from kinematic rupture models. Furthermore, I suggest that when the fault size is much larger than L_c, then most space-time characteristics of slip differ between a rough fault and a corresponding planar fault.

Keywords: Rough faults, Rate-and-state friction, Earthquake cycle simulations, Earthquake statistics, Earthquake ruptures, Pulses
2010 MSC: 00-01, 99-00

1. Introduction

Most modeling studies of earthquakes and the seismic cycle idealize faults as planar surfaces. However, a large body of work has shown that faults and rock surfaces are not planar (e.g. Brown and Scholz, 1985; Power et al., 1987; Power and Tullis, 1991; Sagy et al., 2007; Candela et al., 2012). It has been established that fluctuations from planarity in faults are statistically fractal and self-affine (see Section 1.1 for details). It has become increasingly important to understand how and when planar models accurately capture key characteristics of individual ruptures as well as fault behavior during the entire seismic cycle.

Recently, several studies have simulated earthquakes on fractal faults. In most cases, a single rupture is simulated, where the stress distribution and initial conditions are assumed before artificially nucleating the rupture (Dunham et al., 2011a; Fang and Dunham, 2013; Shi and Day, 2013; Bruhat et al., 2016). These studies have included many of the relevant physics, such as off-fault plasticity and full elastodynamic effects. However, they are too computationally expensive to simulate multiple earthquake cycles, which would include inter-seismic and post-seismic slip, as well as natural nucleation. This means that the assumed initial stress distribution may strongly influence the length and propagation characteristics of the simulated ruptures. A complete approach would ideally allow stresses to evolve naturally over multiple cycles.

Other models have been developed that simulate the whole seismic cycle (Tal et al., 2018; Tal and Hager, 2018a; Ozawa et al., 2019). However, these methods lack a mechanism for stress relaxation, such as off-fault plasticity, and are purely elastic. This means that only a few cycles can be simulated before stresses build-up due to geometric incompatibility

*Corresponding author:
Email address: eheimiss@caltech.edu (Elías Rafn Heimisson)

and reach unrealistic values. These studies cannot investigate behavior over multiple cycles. Recently, Allam et al. (2019) used the RSQsim cycle simulator to simulate seismicity on a self-affine fault over multiple cycles. They used backslip to relax stresses and thus achieve an efficient way to simulate long term fault behavior. However, Allam et al. (2019) used oversized dislocations and did not resolve the relevant length-scales that arise from elasticity and the assumed friction law. Such models generally produce complex behavior that becomes simpler with grid refinement (Rice, 1993; Ben-Zion and Rice, 1997). Since we expect fault roughness to produce complexity, it may be hard to untangle the contribution of the oversized dislocations versus the fault roughness.

Here I show results from a 2D plane-strain boundary element model with frictional properties governed by rate-and-state friction where state evolution evolves according to the aging law (Dieterich, 1979; Ruina, 1983). The simulations are quasi-dynamic and implement a variation of the backslip approach to relax stresses. Thus unlike previous work, I report results from multiple cycles without unrealistic stress build-up, but at the same time, discretization is chosen such that all relevant lengths and time-scales are fully resolved. While many previous studies have focused on the amplitude-to-wavelength ratio of the roughness (e.g. Tal and Hager, 2018b; Bruhat et al., 2016), I focus on systematically varying the minimum roughness wavelength of the fault. The range of λ_{min} explored is from 1/3 to 10 times the nucleation length for a planar fault.

1.1. Background

In this study, I investigate a strictly self-similar and statistically fractal fault. Self-similarity, in this case, implies the root-mean-square (RMS) fluctuations from planarity h_{RMS} are linearly proportional to the fault segment length L (Power and Tullis, 1991), in other words,

$$h_{RMS} = \alpha L, \tag{1}$$

where α is the amplitude-to-wavelength ratio. Faults that obey such self-similarity have a power spectral density (PSD) (Power and Tullis, 1991):

$$P_h(k) = (2\pi)^3\alpha^2|k|^{-3}, \tag{2}$$

where $k = 2\pi/\lambda$ is the wavenumber (λ is the wavelength). Fault roughness is often characterized in terms of the Hurst exponent H, where $h_{RMS} = \alpha L^H$, with $H = 1$ implying strict self-similarity. Fang and Dunham (2013) showed that for a sufficiently long wavelength slip on a self-similar fault, the average resistance to sliding due to geometric complexity is given by the roughness drag:

$$\tau_{drag} = 8\pi^3\alpha^2 \frac{\mu}{1-\nu}\frac{\delta}{\lambda_{min}}, \tag{3}$$

where δ is slip magnitude and λ_{min} is the minimum wavelength that is present in the fault profile (other symbols are defined in Table 1). The spatial extent of the slip patch must be much larger than λ_{min} for this to be valid. Roughness drag can be generalized to self-affine faults (Ozawa et al., 2019), but here I focus on the strictly self-similar case. In Section 3.1.1, I will use roughness drag to understand the certain rupture characteristic of the simulations in a quantitative manner.

Real faults are found to have α in the range of $10^{-3} - 10^{-2}$ (Power et al., 1987). The value likely depends on the maturity (cumulative amount of slip) of a fault, with the upper limit corresponding to less mature faults (Sagy et al., 2007). In this study, I have taken $\alpha = 0.01$, thus possibly representing an immature fault. Computational reasons also motivate this choice of α since it allows interesting effects of the roughness to manifest at smaller length scales. Some studies found fault surfaces to be largely self-affine with $H = 0.8$ in the direction of slip, but with a different slope at other scales (Candela et al., 2012). However, it has been argued that a self-similar scaling ($H = 1$) can well fit all resolvable scales simultaneously (Shi and Day, 2013).

The roughness drag τ_{drag} (Eq. 3) has α^2 dependence on amplitude-to-wavelength ratio, for small α the drag could be assumed small. However, the roughness drag also depends on δ/λ_{min}. Implying that τ_{drag} diverges as $\lambda_{min} \to 0$ for all non-zero values of α. Clearly if λ_{min} is sufficiently small, yielding of the material will occur as δ increases, thus limiting the roughness drag resistance. Fang and Dunham (2013), suggested this may occur when $\delta/\lambda_{min} \approx 1$. The fact that faults are found to be rough over virtually all scales suggests that λ_{min} may be very small and may, therefore, be an important contributor to τ_{drag}, at least up to a point when yielding occurs, that is why I have chosen to focus on λ_{min} in this study.

2. Model Description

I use a boundary element method to mesh a fault surface $h(x)$ (Figure 1). The slip on each element (or dislocation) is assumed to be tangential to $h(x)$ (Figure 1d). That is, the dislocation is tilted at an angle $\theta = \arctan(dh/dx)$. Using analytical solutions for elastic dislocations in full-space (Nikkhoo et al., 2016) I compute a matrix of influence coefficients that relate slip vector $\boldsymbol{\delta}$ and changes in shear $\boldsymbol{\tau}$ and normal stress $\boldsymbol{\sigma}$ at the center of each dislocation:

$$\boldsymbol{\tau}' = \boldsymbol{G}_\tau \boldsymbol{\delta}' \text{ and } \boldsymbol{\sigma}' = \boldsymbol{G}_\sigma \boldsymbol{\delta}', \tag{4}$$

where the meaning of $\boldsymbol{\delta}'$ versus $\boldsymbol{\delta}$ is discussed later. The matrices of influence coefficients are compressed using the H-matrix approach of Bradley and Segall (2011). The frictional interface is governed by rate-and-state friction and aging law, respectively:

$$\frac{\tau_0 + \boldsymbol{\tau}' - \eta \boldsymbol{V}}{\sigma_0 + \boldsymbol{\sigma}'} = f_0 + a \log\left(\frac{\boldsymbol{V}}{V_0}\right) + b \log\left(\frac{V_0 \boldsymbol{\theta}}{d_c}\right) \tag{5}$$

$$\dot{\boldsymbol{\theta}} = 1 - \frac{\boldsymbol{\theta} \cdot \boldsymbol{V}}{d_c}, \tag{6}$$

where $\boldsymbol{V}$ and $\boldsymbol{\theta}$ represent the slip speed and state at the center of each dislocation respectively.

An infinite planar fault with the same frictional properties will oscillate around V_0 as long as the long term average of the elastic stress transfer is $\boldsymbol{\tau}' = 0$. This is reasonable; otherwise, the long term average velocity of the fault would be changing, which can only occur if the loading is changed. The problem is more complicated for a non-planar and/or

Table 1: Reference parameters that are kept constant in the study

Symbol	Description	Value
Material properties		
ν	Poisson's ratio	0.25
μ	Shear modulus	30 GPa
c_s	Shear wave speed	3.5 km/s
Friction		
d_c	Characteristic state evolution distance	100 μm
a	Rate dependence of friction	0.01
b	State dependence of friction	0.0125
V_0	Steady state sliding velocity	10^{-9} m/s
f_0	Steady state coefficient of friction at V_0	0.6
σ_0'	Initial effective normal stress	100 MPa
Fault		
α	Amplitude-to-wavelength ratio	0.01
L	Fault length along x-axis	10 km
Other parameters dependent on parameters above		
L_∞	Critical crack half-length	$\frac{\mu d_c}{\pi(1-\nu)\sigma_0 b} \cdot \left(\frac{b}{b-a}\right)^2 \approx 29.3825\,\mathrm{m}\dagger$
$b-a$	Degree of rate-weakening	0.0025
η	Radiation damping	$\mu/(2c_s) \approx 4.2857\,\mathrm{MPa}\cdot\mathrm{s/m}\dagger\dagger$
τ_0	Initial shear stress	$f_0\sigma_0 + \eta V_0 \approx 60.0000\,\mathrm{MPa}$
θ_0	Initial state	$d_c/V_0 \cdot (1 + \mathcal{N}(0, 0.01))$
Notes		
†	(Rubin and Ampuero, 2005)	
††	(Rice, 1993)	
$\mathcal{N}(m,s)$	Gaussian noise, mean m, std. s	

finite faults if the medium doesn't relax the stresses, which is the case for a perfectly elastic solid, then as $\boldsymbol{\delta}$ increases so do the stress magnitudes. However, the stresses in the medium and on the fault must, on average, relax at the same rate as the loading rate. Otherwise, they would simply build up indefinitely. I approximate this process using the backslip approach (Richards-Dinger and Dieterich, 2012), where I have defined $\boldsymbol{\delta}' = \boldsymbol{\delta} - V_0 t$. Which is then used in Eq. 4 to compute the elastic stress transfer. This approach differs from the RSQsim backslip implementation (Richards-Dinger and Dieterich, 2012; Allam et al., 2019), since I do not have to slip the faults backward to determine the backslip stressing rate. I've simply formulated the problem such that the average steady-state speed on the fault at any point V_0 is also the loading rate. In this manuscript, I will plot $\boldsymbol{\delta}$ instead of $\boldsymbol{\delta}'$ to show cumulative slip with time. This gives the illusion that the edges of the finite fault are moving and continuously generating stress concentrations. However, this is not the case since $\boldsymbol{\delta}'$ is used to compute the stress transfer.

The fault profile (Figure 1) is stochastically generated with a power spectral density in Eq. 2 using the implementation of Dunham et al. (2011a). The dislocation length projected on the x-axis was set to 1 m. The smallest $\lambda_{min} \approx 10$ m and is thus resolved in the simulations. Frictional properties (see Table 1) are set such that the crack half-length, which marks the transition from nucleation to a dynamic instability, is constant $L_\infty \approx 30$ m and is therefore also well resolved. The fault profile was generated with λ_{min} ranging from $L_\infty/3$ to $10 \cdot L_\infty$, but in all cases with the same random seed such that the Fourier decomposition at larger wavelengths is identical in both magnitude and phase.

2.1. Algorithm

The $n+1$ time-step of the simulations starts by computing shear and normal stress using the slip of the previous time step: $\boldsymbol{\tau}'_{n+1} = \boldsymbol{G}_\tau \boldsymbol{\delta}'_n$ and $\boldsymbol{\sigma}'_{n+1} = \boldsymbol{G}_\sigma \boldsymbol{\delta}'_n$, where $\boldsymbol{\tau}_{n+1} = \tau_0 + \boldsymbol{\tau}'_{n+1}$ and $\boldsymbol{\sigma}_{n+1} = \sigma_0 + \boldsymbol{\sigma}'_{n+1}$. Furthermore, a prediction of the $n+1$ value of the state variable is made:

$$\boldsymbol{\theta}^* = \boldsymbol{\theta}_n + \mathrm{d}t_n \left(1 - \boldsymbol{\theta}_n \cdot \boldsymbol{V}_n / d_c\right). \tag{7}$$

Now Eq. 5 can be rearranged to provide an approximation for the slip speed at time step $n+1$ given that the relevant fields are known at time step n.

$$\boldsymbol{V}_{n+1} = V_0 \exp\left(\frac{\boldsymbol{\tau}_{n+1} - \eta \boldsymbol{V}_n}{a\boldsymbol{\sigma}_{n+1}} - f_0/a - \frac{b}{a}\log(V_0\boldsymbol{\theta}^*/d_c)\right), \tag{8}$$

At high slip speeds (~ 1 cm/s) where inertial effects become important, Eq. 8 is not accurate and generates numerical dispersion. At dislocation centers that satisfy ($\boldsymbol{V_n} > 1$ cm/s) I solve for $\boldsymbol{V_{n+1}}$ by using Eq. 9.

$$\left|\boldsymbol{V}_{n+1} - V_0 \exp\left(\frac{\boldsymbol{\tau}_{n+1} - \eta \boldsymbol{V}_{n+1}}{a\boldsymbol{\sigma}_{n+1}} - f_0/a - \frac{b}{a}\log(V_0\boldsymbol{\theta}^*/d_c)\right)\right| = 0 \tag{9}$$

Remarkably, Eq. 9 only needs to be solved approximately to suppress dispersion and attain a convergent and sufficiently accurate solution. I perform a grid search of 15 values ranging from $0.98V_n$ to $1.03V_n$ (including V_n) and select the answer closest to the solution. Using a more refined grid search did not improve the results. This crude grid search allows for efficient simulations of dynamic events.

Next step updates the state-variable and slip using the following equations:

$$\boldsymbol{\theta}_{n+1} = \boldsymbol{\theta}_n + \mathrm{d}t_n\left(1 - \boldsymbol{\theta}_n \cdot \boldsymbol{V}_{n+1}/d_c\right), \tag{10}$$

$$\boldsymbol{\delta}_{n+1} = \boldsymbol{\delta}_n + \mathrm{d}t_n \boldsymbol{V}_{n+1}. \tag{11}$$

The final step determines the new time-step

$$\mathrm{d}t_{n+1} = \min([\epsilon d_c/\max(\boldsymbol{V}_{n+1}), \epsilon \min(\boldsymbol{\theta}_{n+1})]). \tag{12}$$

where ϵ is adjusted such that stability and convergence is found, for this study it was set to 1/64. The problem is initialized such that $\boldsymbol{\tau} = \tau_0$, $\boldsymbol{\sigma} = \sigma_0$ and $\boldsymbol{\theta} = d_c/V_0(1 + \mathcal{N}(0, 0.01))$ at all dislocation centers (See Table 1). The fault is thus approximately at steady state $\boldsymbol{V} = V_0$ initially apart form small amplitude Gaussian white noise added to the initial state. The noise is generated using the same random seed and is thus the same for all simulations. In this study I explore the statistics of event sizes for simulations that spans multiple cycles.

Each simulation is run for 6.4 million time steps, but one simulation ($\alpha = 0$) was extended to exceed 100 seismic events. The only difference between each simulation is λ_{min}. I thus do not generate statistic by simulating one event on multiple stochastic realizations of a rough fault profile as has been explored previously (e.g. Fang and Dunham, 2013).

Convergence tests for the slip and slip speed at a given time step, and timing that the first event reached a slip speed larger than 1 m/s all revealed slightly better than 1st order convergence as ϵ was decreased (see Supplementary Material for details on convergence tests). It is worth noting that more complex higher-order time-stepping algorithms have been developed (e.g. Lapusta et al., 2000; Lapusta and Liu, 2009). The algorithm was tested by reproducing benchmarks reported by Erickson et al. (2020) (see Supplementary Material for details on benchmarking). This test revealed that a highly spatially refined cycle simulation carried out using a spectral boundary integral method (SBIM) (Lapusta et al., 2000; Lapusta and Liu, 2009) could be reproduced in great detail with 1/4 less spatial resolution. The SBIM resolved the cohesive zone (e.g. Day et al., 2005; Ampuero and Rubin, 2008; Lapusta and Liu, 2009) by 6 elements, whereas the algorithm described here attained the same results with only 1.5 elements resolving the cohesive zone. This suggests that the boundary integral approach taken here may only need to resolve the cohesive zone by 1.5 elements. For rough faults, the slip and normal stress are coupled, and the length of the cohesive zone is not well understood. If the value for a planar fault is taken as representative, then the simulations here resolve the cohesive zone by 3 elements, which was found sufficient for the SBIM (Day et al., 2005). Generally, the normal stress in the simulations reported here does not exceed %50 of σ_0, and it thus likely reasonably well resolved. This is supported by the convergence of the aforementioned metrics with decreasing ϵ and would likely not converge if the cohesive zone was poorly resolved (Day et al., 2005).

In this study, I investigate a limit where the fault is much larger than the nucleation length, and chaotic behavior is expected (Barbot, 2019). Further, in this case, slip and normal stress are coupled; this additional coupling will likely expedite any chaotic divergence. It is thus important to note that all simulations, no matter how accurate the numerical solution, will appear to be non-convergent with spatial or temporal refinement if simulated

166 for long enough. We can thus only interpret the long term fault behavior in a statistical or
167 collective sense.

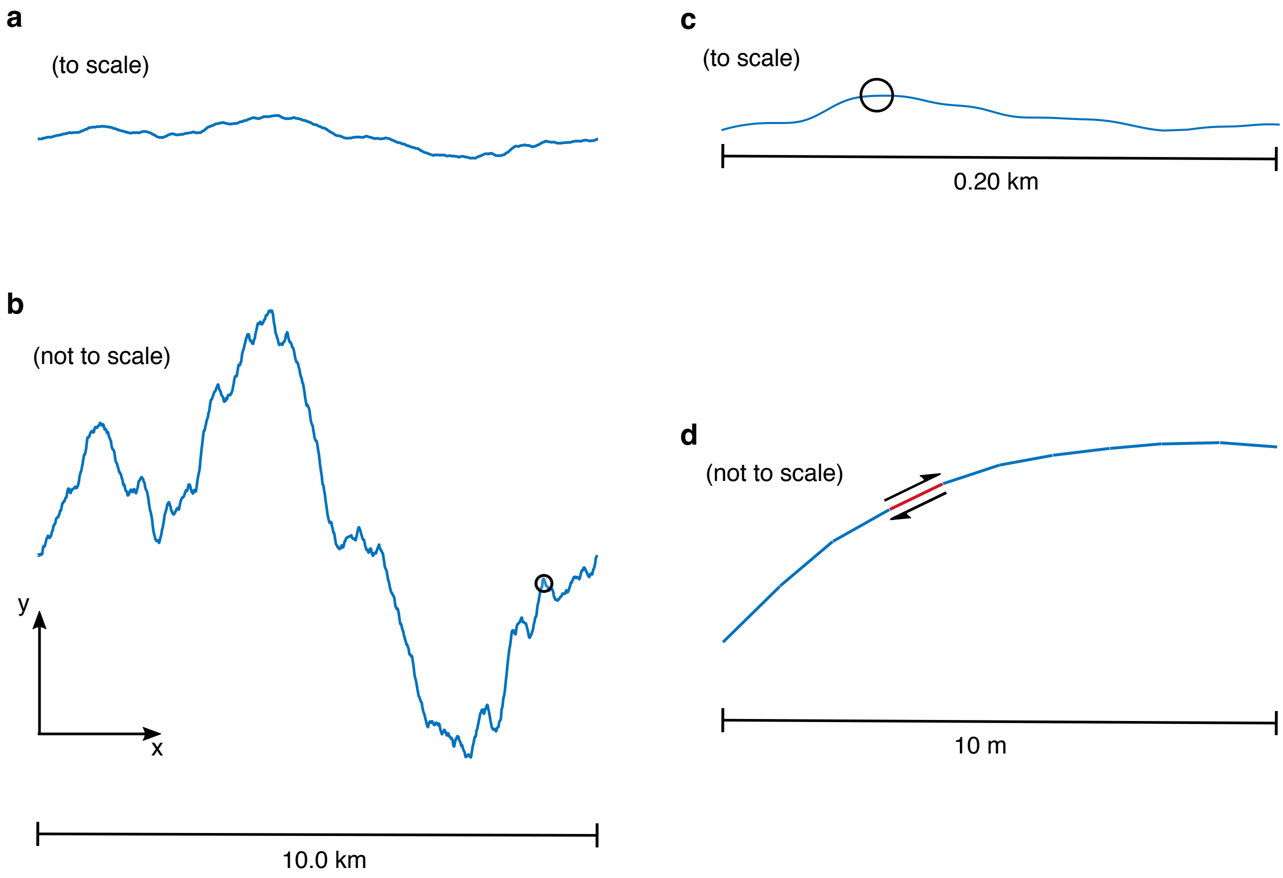

Figure 1: Fault profile at various scales for $\lambda_{min} = 2L_\infty/3$. **a** shows the entire fault at the correct length to amplitude ratio. **b** same as **a** except with exaggerated amplitude. Small circle shows the location of the fault segment shown in **c**. Circle in **c** shows the fault segment shown in **d** which displays the length scale of the discretization. Red segment shows the length of one dislocation sliding tangentially to the fault topography. It is assumed that the fault cannot open or interpenetrate.

168 ## 3. Results

169 ### *3.1. Rupture characteristics*

170 We start by visualizing the cumulative slip in all simulations (Figures 2, 3 and 4)

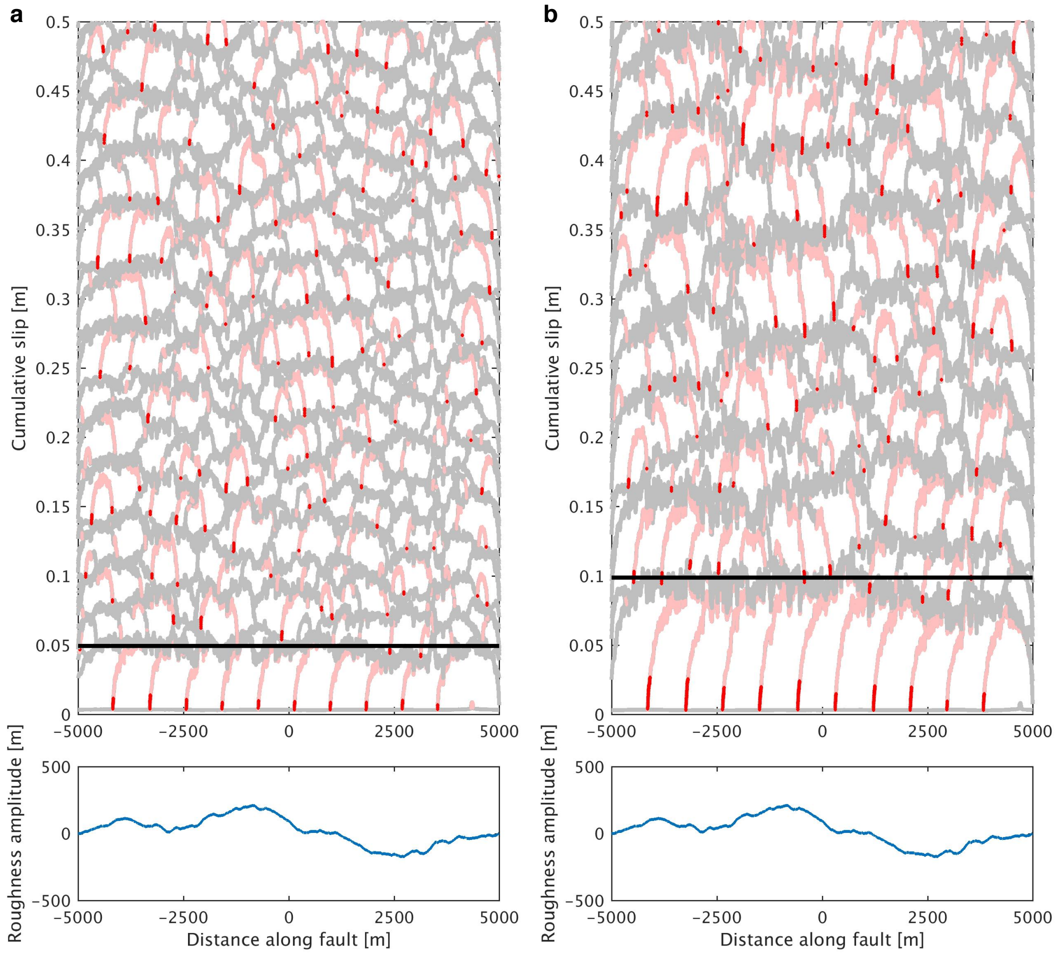

Figure 2: Snapshots of cumulative slip as a function of distance along fault. Red lines indicate points slipping faster than 1 m/s, pale pink lines indicate slip speeds larger than 1 cm/s. Grey lines are points slipping $\leq$ 1 cm/s. **a** shows results for $\lambda_{min} = L_\infty/3$, **b** shows results for $\lambda_{min} = 2L_\infty/3$. Bottom panels shows corresponding fault roughness, at the scale shown the fault profiles appear identical. Black line is the estimate of δ_c, the maximum slip distance estimate discussed in Section 3.1.1. This slip shown corresponds to approximately 16 years of activity.

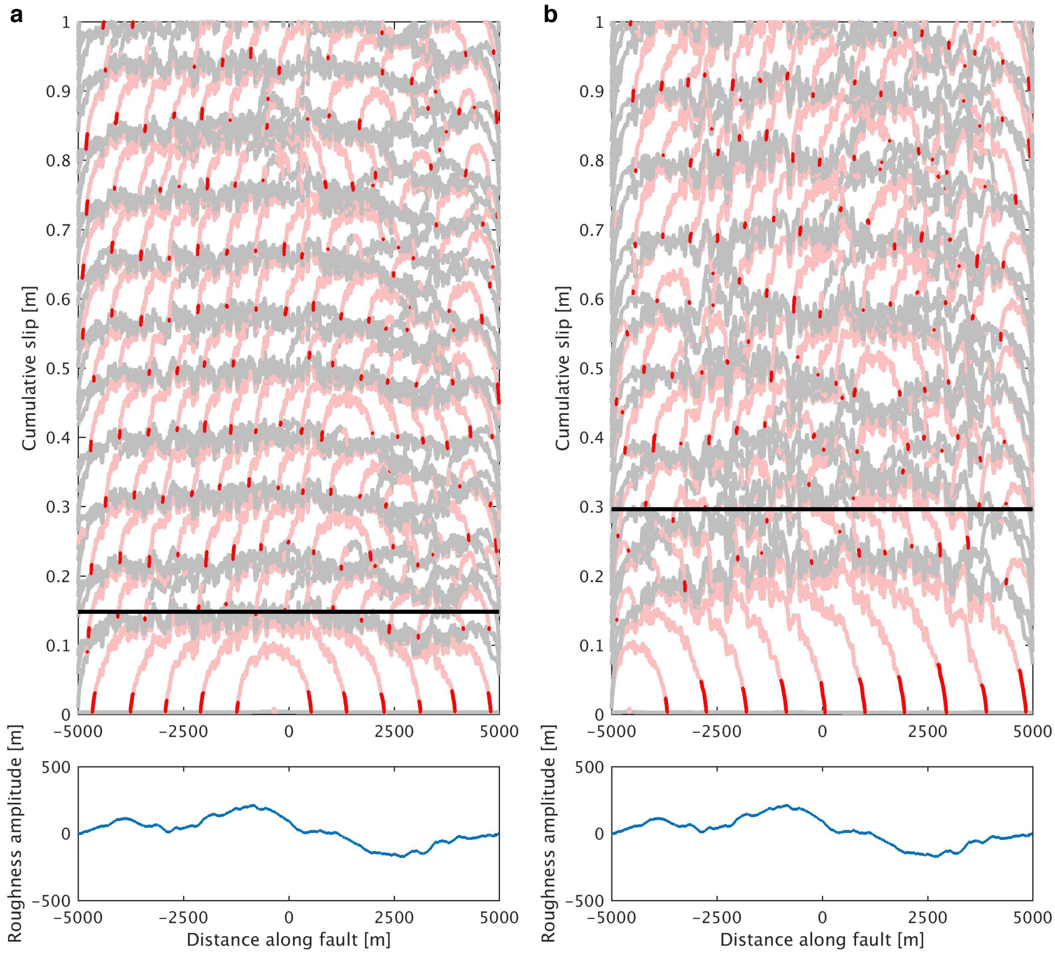

Figure 3: Same as Figure 2 except **a** shows results for $\lambda_{min} = L_\infty$, **b** shows results for $\lambda_{min} = 2L_\infty$. Note that the cumulative slip scale is different compared to Figure 2. This slip shown corresponds to approximately 32 years of activity.

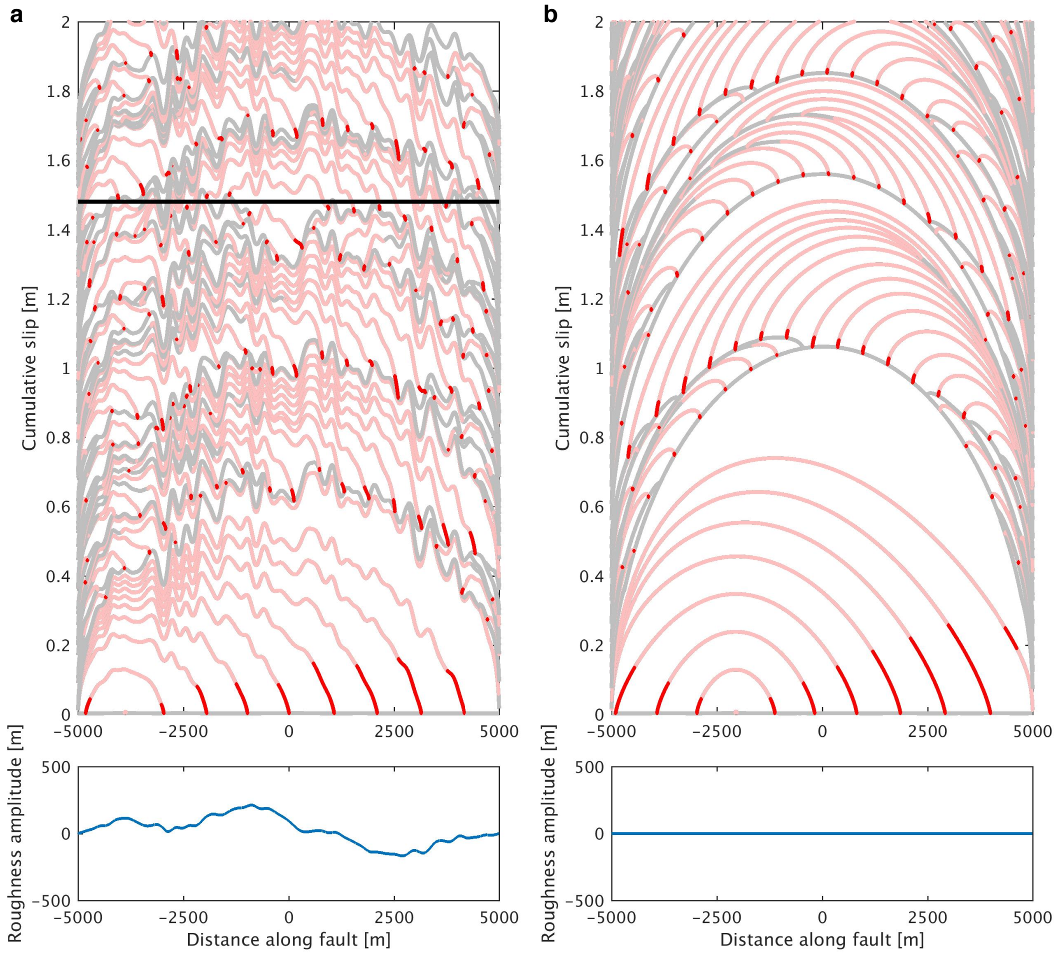

Figure 4: Same as Figure 2 except **a** shows results for $\lambda_{min} = 10L_\infty$, **b** shows a reference simulation of a planar fault. Note that the cumulative slip scale is different compared to Figures 2 and 3. No δ_c value exists for a planar fault and maximum slip distance is determined by fault finiteness and frictional properties, for **a** δ_c, significantly over-predicts the maximum slip distance because fault finiteness becomes the limiting factor before slip reaches δ_c. This slip shown corresponds to approximately 63 years of activity.

From the slip profiles above, we observe that the initial rupture always propagates the whole length of the fault. However, later events tend to be partial ruptures except when λ_{min} is large (Figure 4). Initially, the shear and normal stresses are selected to be spatially uniform, and the stress changes due to geometric complexity induced by the actively propagating rupture are not sufficient to arrest the rupture. Once the initial rupture has terminated, the resulting heterogeneous stress field can arrest ruptures and limits the event sizes. The results thus suggest that the assumed initial stress field in single rupture simulations on rough faults may be the primary control on the resulting rupture dimensions.

Another important observation from the simulations is that if events become sufficiently large, they transition from being crack-like to pulse-like, once they transition to pulse-like propagation, the events lock in an approximately fixed amount of slip. This is clear in simulations reported in Figures 2 and 3, whereas the fault in Figure 4a isn't sufficiently large to show this transition and is qualitatively similar to the planar fault simulation (Figure 4b). The crack to pulse transition suggests that ruptures may have reached a length scale at which roughness drag becomes important (Eq. 3). In the next subsection, I further analyze the transition from a crack to a pulse.

3.1.1. Crack to pulse transition

Let us hypothesize that transition from crack to pulse occurs approximately when the stress drop is equal to the roughness drag $\Delta\tau = \tau_{drag}$. Under these conditions it cannot be energetically favorable for a fault patch to slip further. Assuming a simple constant stress drop in-plane crack of half-length L_c then $\Delta\tau = (2\mu\bar{\delta})/(\pi(1-\nu)L_c)$, where $\bar{\delta}$ is the average slip. Setting $\Delta\tau = \tau_{drag}$ provides:

$$L_c = \frac{\lambda_{min}}{4\pi^4\alpha^2}, \tag{13}$$

which we interpret as a characteristic length scale for the crack to pulse transition. Remarkably, this scale only depends on roughness parameters λ_{min} and α^2 and not mechanical properties of the host rock and not the friction law, as long as the friction law favors instabilities that become crack-like. By comparing L_c to slip speed profiles during pulse-like propagation, we find that L_c well characterizes the dimension of the slip patch that is slipping approximately fast enough to radiating seismic energy (Figure 5). We may thus consider L_c as a characteristic dimension of the pulse. These results suggest that we may estimate L_c and therefore λ_{min}/α^2 from dynamic slip models that resolve pulse-like propagation (e.g. Galetzka et al., 2015). However, it is worth noting for a 3D rough surface L_c may be different, at least in terms of prefactor. Further, other mechanisms can result in the manifestation of slip pulses on faults, such as low-stress conditions (Zheng and Rice, 1998), or linear stability at large wavelengths due to slip to normal stress coupling (Heimisson et al., 2019), which may be responsible for generating the observed pulses in nature. It can be shown, although omitted here, that by including roughness drag in a linearized stability analysis using rate-and-state friction (e.g. Rice et al., 2001), that large wavelengths become stable (although not related to normal stress changes). This also gives a length scale $\propto \lambda_{min}/\alpha^2$, albeit with a different prefactor than L_c.

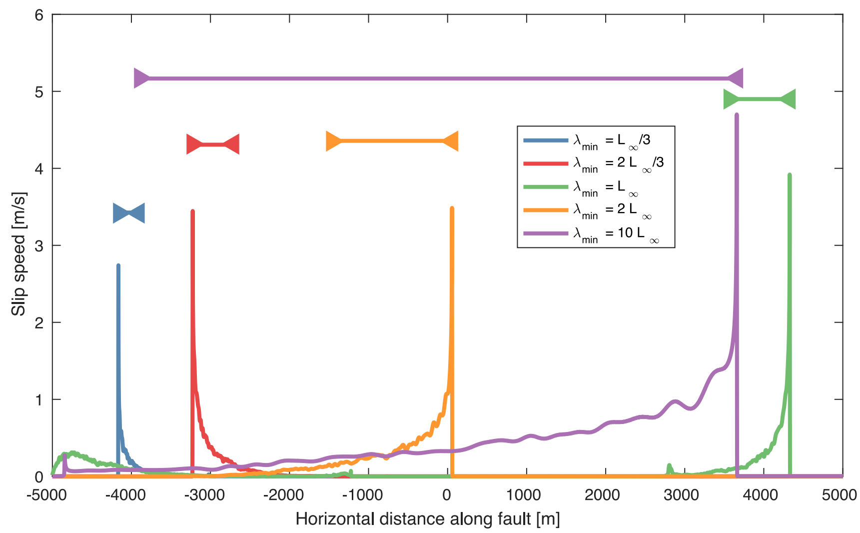

Figure 5: Comparison of L_c (horizontal lines, Eq. 13) to snapshots of slip speeds during pulse-like propagation during each simulation. The figure suggests that L_c is a good measure of a characteristic pulse length.

We may now use details of the rate-and-state friction law to estimate the maximum slip distance during pulse-like propagation. Once pulse reaches a point on the fault, we expect that friction rabidly evolves towards steady-state (Rubin and Ampuero, 2005). Locally the stress drop can be approximated as $\Delta\tau_{RS} \approx (b-a)\sigma_0 \log(V_d/V_0)$, where V_d could be considered a peak slip speed, here we shall take $V_d = 5$ m/s, thus $\log(V_d/V_0) \approx 22.3$. By virtue of the slow growth of the logarithm function, a minor error is introduced even if V_d is an order of magnitude smaller (in which case $\log(V_d/V_0) \approx 20.0$). Equating $\Delta\tau_{RS} = \tau_{drag}$

reveals a maximum slip distance δ_c before we expect roughness drag to prevent further slip

$$\delta_c = \lambda_{min} \frac{1-\nu}{\mu} \frac{(b-a)\sigma_0 \log(V_d/V_0)}{8\pi^3\alpha^2}, \tag{14}$$

which suggests that in a single event, $\delta \lesssim \delta_c$. The corresponding values of δ_c are plotted as black horizontal lines in Figures 2, 3 and 4 for each simulation and show excellent agreement with the slip magnitude in the initial event in all cases where the fault was sufficiently large to manifest the crack to pulse transition properly. However, following the initial event slip rarely reaches δ_c, due to heterogeneity and that the average stress on the fault is typically lower than initially when the first event nucleates. This suggests that the slip only reaches δ_c under very favorable conditions. The crack to pulse transition reported here resembles the changes in the slip distribution of simple static crack calculations done by Dieterich and Smith (2009) as the crack size was increased. They also reported a maximum slip distance with the same dependence on λ_{min}/α^2 as Eq. 14. However, their formulation included an unknown fitting coefficient, whereas no fitting is done here.

3.2. Seismicity and statistics

As seen in Figures 2, 3 and 4 a single rough or planar fault can host a large distribution of event sizes. In this section, I investigate the characteristics and statistics of the seismicity in each simulation, in particular, the seismic moment distribution.

To extract discrete events from the simulations some assumptions need to be made about the dimension and timing of each event. The following criteria are used for identifying a single event and estimate seismic moment.

1. Identify a time period where the fault continuously slips at any point faster than 10 cm/s.
2. Find points where slip during that time was larger than d_c.
3. Compute the length of rupture and square to get area.
4. Compute the average change in slip where slip exceeded d_c.
5. Compute the seismic moment and magnitude

Clearly squaring the length of a rupture to obtain area is very simplistic and is only valid if the aspect ratio of the ruptures are constant and other 3D effects, such as those that might arise from event interactions, can be ignored. However, this provides a systematic way to compare our in-plane simulations to 3D observations.

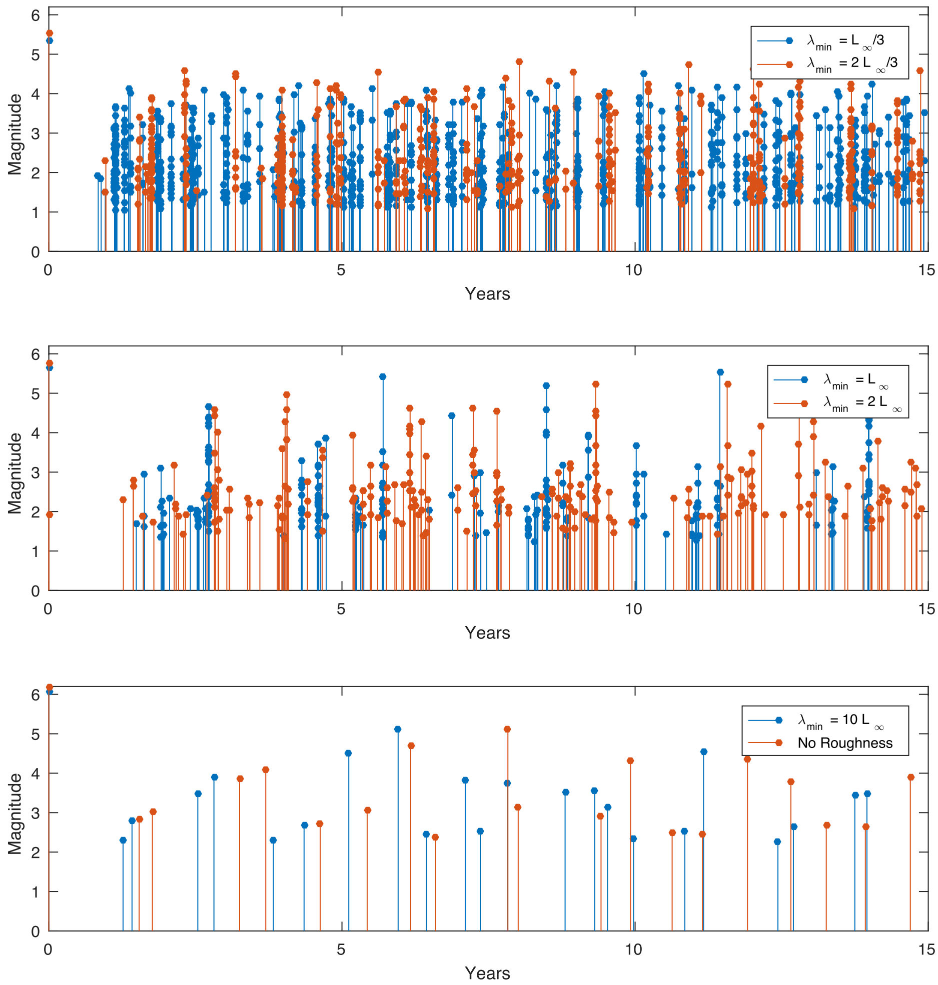

Figure 6: Magnitude versus time in all simulations for the first 15 years of simulations. For small λ_{min}, events are generally smaller and more numerous compared to larger λ_{min} values. Comparison of $\lambda_{min} = 10L_\infty$ and the no-roughness simulation reveals qualitatively similar behavior. The simulations indicated that there is both a maximum and minimum magnitude of events, which change with λ_{min}. The figure only shows the first 15 years of each simulation to illustrate the differences in temporal characteristics and clustering. The bottom plot appears to have smaller events than the middle plot; this is due to the large moment that is released in the first event. Later when stress builds up the smoother faults will generate larger events. See Figure S4 in the Supplementary Material for a corresponding plot of all simulated events.

Figure 6 reveals very different frequency and magnitudes of seismicity for cases where λ_{min} is smaller or comparable to L_∞. For $\lambda_{min} = 10L_\infty$, the results suggest that the rough fault and planar fault are qualitatively similar in terms of the frequency, timing, and magnitudes of event. Further, Figure 6 suggests that each simulation has a minimum and maximum moment event. The maximum moment is easy to understand since slip cannot exceed δ_c (Eq. 14), and the fault has a finite length. The minimum moment size is more mysterious since by decreasing λ_{min} the minimum moment also decreases. However, by decreasing λ_{min} the nucleation dimension should increase (Tal et al., 2018), which suggests that the smallest event size might also increase. A possible explanation comes from Eq. 14 where the slip distance is reduced, thus limiting the sizes of the events. That explanation is not fully satisfying since the smallest events in the simulations tend to arrest before reaching a slip distance similar to δ_c. A more likely explanation may be that due to residual stress. If λ_{min} is decreased, the normal stress is locally increased at shorter wavelengths, and locally, the nucleation dimension is reduced. This finding highlights the importance of the initial stress in the analysis of earthquake nucleation on rough faults.

If the simulations presented, have any resemblance to earthquakes in nature, we expect that the moment distribution of events to be a power-law. Let us compare the empirical probability distribution function (PDF) to a theoretical moment distribution (Kagan, 2002):

$$\mathrm{PDF}(M) = \frac{M_{max}^{\beta} M_{min}^{\beta}}{M_{max}^{\beta} - M_{min}^{\beta}} \beta M^{-1-\beta}, \text{ where } M_{min} \leq M \leq M_{max}, \tag{15}$$

where M is the moment and $\beta = 2b/3$, with b being the b value of the Gutenberg-Richter distribution, where typically $b \approx 1$. For comparison with simulation, we have chosen a truncated moment distribution since we have inferred that each simulation has both a minimum and maximum moment. Comparison of the theoretical PDF (Eq. 15) and the empirical PDF determined from each simulation shows that the two are generally in good agreement for $b = 0.5$ (Figure 7), which well characterizes the fall-off with increased moment. It generally appears λ_{min} does not control the fall-off, but as has been previously noted, the truncation of the distribution is changed by λ_{min}. It is notable that even for the no-roughness limit, the events follow the same power-law distribution. This is consistent with recent work (Cattania, 2019), which showed in simulations and theory that a planar fault that is sufficiently large could manifest a power-law distribution of events (see further discussion in Section 4.1).

Some interesting differences are found in Figure 7, when comparing the cases of $\lambda_{min} \lesssim L_\infty$ to $\lambda_{min} = 10L_\infty$ and the no-roughness case. We notice that at low moment bins, the empirical distribution has gaps for $\lambda_{min} = 10L_\infty$ and the no-roughness case, whereas all gaps for $\lambda_{min} \lesssim L_\infty$ occur at high moment bins when events are rare. The latter is most likely due to biased sampling. The synthetic catalog includes approximately the maximum event size since it is the first event that occurs (Figure 2, 3 and 4), but due to very numerous small events that increase computational time in these cases, it was not feasible to simulate long enough sequences that would realize these rare events. However, for $\lambda_{min} = 10L_\infty$ and the no-roughness case, gaps occur at event sizes that should have been realized in the catalog. For a larger L/L_∞ ratio, these gaps might disappear. The gaps in the PDF for a planar fault in Figure 7 are consistent with the bifurcation diagrams by Barbot (2019), which suggest that certain values of intermediate seismic moments do not occur. Based on the results in this paper, I hypothesize that rough faults may be ergodic in the sense that if a single simulation is run for long enough, then events of all possible moments are realized. However, a planar fault simulation will only realize a subset of the distribution of possible moments and are thus not ergodic. I conclude that more study of this topic is needed, in particular in 3D.

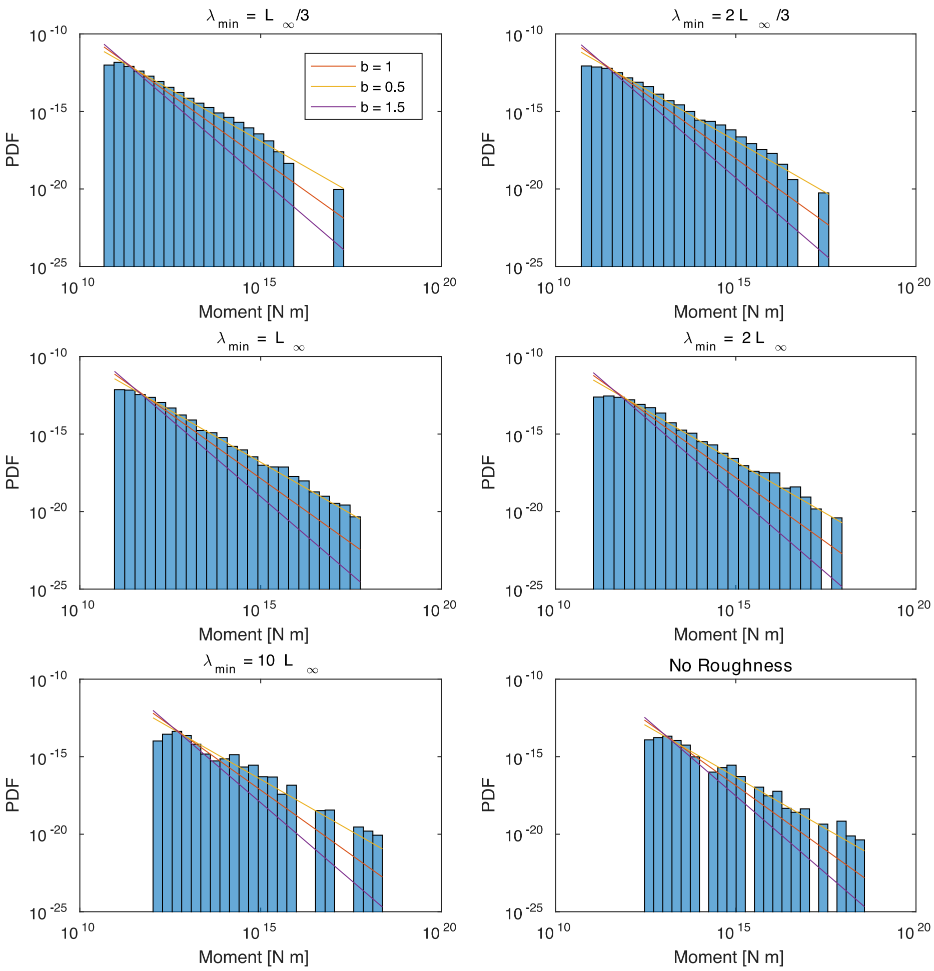

Figure 7: Comparison of Eq. 15 and the empirically estimated moment PDF function. The maximum and minimum moments in Eq. 15 are taken as the observed maximum and minimum moments in the simulations. Eq. 15 is plotted for $b = 0.5, 1, 1.5$, the comparison shows that a good agreement between empirical and theoretical PDFs is found for $b = 0.5$. Empirical PDFs for $\lambda_{min} = L_\infty/3$, $2L_\infty/3$, L_∞, $2L_\infty$, $10L_\infty$, and no roughness simulations are based on 1164, 974, 804, 590, 110, 142 events respectively.

75

4. Discussion

4.1. The b value

The b value most consistent with the simulations seems to be $b = 0.5$, which is considerably smaller than the typically observed value of $b = 1$ value. The results suggest that the value is not related to the roughness since the same value is found for a planar fault, at least for $H = 1$. Cattania (2019) analyzed an anti-plane fault loaded from below by a creeping velocity strengthening section and bounded from above by a free surface. Through theoretical considerations of simple crack models, she argued $b = 3/4$, which was supported by simulations. This value is also somewhat smaller than typically observed. Cattania (2019) squared the rupture lengths to attain an area, as was done here. The simplistic treatment of the 3D effect is thus not the source of the difference, although it may factor into what value of b is determined from the simulations. The main difference in this study compared to Cattania (2019) is in the fault loading, here I have simulated a finite in-plane fault that is loaded using backslip, whereas Cattania (2019) loaded by deep creep and stress build-up at the top was prevented by a free surface. I suggest that the difference in loading is likely the cause of the difference in b value, but I conclude that this issue needs further attention since it may provide insight into the physical interpretation of b.

4.2. The backslip approach

The backslip approach to loading and relax stresses is a very efficient way of simulating earthquake cycles for geometrically complex faults. One can argue that stresses on and off faults in the earth must relax on average over multiple cycles at the same rate as the stresses build-up due to loading. Otherwise, stress accumulation would diverge. The backslip approach achieves this balance. However, the transient temporal and spatial evolution of the stresses may not be as expected from a more rigorous model that considers off-fault plasticity using a continuum model of plasticity (e.g. Dunham et al., 2011b,a; Shi and Day, 2013). However, such continuum plasticity models may not be able to accurately represent an important source of relaxation that occurs off the main fault on discrete structures such as fault branches (Ma and Elbanna, 2019). Further developments of earthquake cycle simulations are needed before we can efficiently simulate multiple cycles on rough faults with realistic stress relaxation mechanisms; in the meantime, backslip offers a simple way to investigate these problems.

4.3. A planar fault approximation

Some of the most efficient earthquake cycle simulators are not simply extended to a rough fault geometry (e.g. Lapusta et al., 2000; Lapusta and Liu, 2009). It is, therefore, worth commenting on if fault roughness can be incorporated in an approximate sense. One simple idea would be to incorporate the pre-stress that, in some statistical sense, is expected from repeated multiple cycles on a rough fault; however, that is not sufficient. The results reported here suggests that roughness drag (Fang and Dunham, 2013) explains key characteristics of earthquake ruptures on rough faults (see also Tal et al., 2018; Ozawa et al., 2019). Importing the correct stress distribution to a planar fault will not describe the influence of roughness drag. Fortunately, roughness drag could be incorporated in a similar manner as radiation damping is included in a quasi-dynamic simulation. For example,

$$\tau = \tau_0 + \tau_{el}(t, \delta) + \tau_l(t) - \eta V - \frac{8\pi^3\alpha^2\mu}{(1-\nu)\lambda_{min}}\delta, \tag{16}$$

where $\tau_{el}(t, \delta)$ is the stress from elastic interaction or wave-mediated stress transfer on a planar fault, and $\tau_l(t)$ represents externally imposed loading of the fault (see Table 1 for other definitions).

5. Conclusions

Roughness has an important influence on both individual ruptures and frequency and magnitude characteristics of events. Events start as crack-like ruptures, but due to roughness drag, they transition to pulse-like ruptures at a characteristic length-scale, L_c, determined by fault roughness alone (Eq. 13). I suggest that slip on faults much larger than L_c cannot be approximated using a planar fault without, at least, including roughness drag (Eq. 16). Pulses lock in approximately spatially fixed slip distance. The maximum slip, δ_c, during pulse-like rupture is set by roughness drag but also depends on the assumed friction law and material properties. I conclude that fault roughness offers a plausible and general mechanism for earthquakes to transition from cracks to pulses as they grow. I find that decreasing λ_{min}, decreases both the maximum and minimum event sizes observed in the cycle simulations;

however, it does not appear to alter the inferred b values, which remains the same even for a reference simulation using a planar fault. Much more numerous small events thus characterize simulations with small λ_{min}, and thus more heterogeneous stress, compared to large λ_{min} or planar fault simulations. The first event in the simulations always ruptures the entire fault, but the following events are generally smaller partial ruptures. This difference suggests that the residual stresses induced by fault roughness are paramount in determining subsequent events sizes. Caution is needed when selecting the initial stress distribution for single rupture models on rough faults since it may significantly influence event sizes.

6. Acknowledgements

I want to thank Eric M. Dunham and Valere Lambert for helpful discussions and two reviewers for their constructive remarks. I partially conducted this research while being supported by NASA Headquarters under the NASA Earth and Space Science Fellowship Program (Grant NNX16AO40H).

References

References

Allam, A., Kroll, K., Milliner, C., Richards-Dinger, K., 2019. Effects of fault roughness on coseismic slip and earthquake locations. Journal of Geophysical Research: Solid Earth doi:10.1029/2018JB016216.

Ampuero, J.P., Rubin, A.M., 2008. Earthquake nucleation on rate and state faults – aging and slip laws. Journal of Geophysical Research: Solid Earth 113. doi:10.1029/2007JB005082.

Barbot, S., 2019. Slow-slip, slow earthquakes, period-two cycles, full and partial ruptures, and deterministic chaos in a single asperity fault. Tectonophysics 768, 228171. doi:https://doi.org/10.1016/j.tecto.2019.228171.

Ben-Zion, Y., Rice, J.R., 1997. Dynamic simulations of slip on a smooth fault in an elastic solid. Journal of Geophysical Research: Solid Earth 102, 17771–17784. doi:10.1029/97JB01341.

Bradley, A., Segall, P., 2011. Efficient numerical modeling of 3d, half-space, slow-slip and quasi-dynamic earthquake ruptures, in: AGU Fall Meeting Abstracts.

Brown, S.R., Scholz, C.H., 1985. Broad bandwidth study of the topography of natural rock surfaces. Journal of Geophysical Research: Solid Earth 90, 12575–12582. doi:10.1029/JB090iB14p12575.

Bruhat, L., Fang, Z., Dunham, E.M., 2016. Rupture complexity and the supershear transition on rough faults. Journal of Geophysical Research: Solid Earth 121, 210–224. doi:10.1002/2015JB012512.

Candela, T., Renard, F., Klinger, Y., Mair, K., Schmittbuhl, J., Brodsky, E.E., 2012. Roughness of fault surfaces over nine decades of length scales. Journal of Geophysical Research: Solid Earth 117. doi:10.1029/2011JB009041.

Cattania, C., 2019. Complex earthquake sequences on simple faults. Geophysical Research Letters 0. doi:10.1029/2019GL083628.

Day, S.M., Dalguer, L.A., Lapusta, N., Liu, Y., 2005. Comparison of finite difference and boundary integral solutions to three-dimensional spontaneous rupture. Journal of Geophysical Research: Solid Earth 110. doi:10.1029/2005JB003813.

Dieterich, J.H., 1979. Modeling of rock friction: 1. experimental results and constitutive equations. Journal of Geophysical Research: Solid Earth 84, 2161–2168. doi:10.1029/JB084iB05p02161.

Dieterich, J.H., Smith, D.E., 2009. Nonplanar faults: Mechanics of slip and off-fault damage, in: Mechanics, structure and evolution of fault zones. Springer, pp. 1799–1815. doi:10.1007/s00024-009-0517-y.

Dunham, E.M., Belanger, D., Cong, L., Kozdon, J.E., 2011a. Earthquake ruptures with strongly rate-weakening friction and off-fault plasticity, part 2: Nonplanar faults. Bulletin of the Seismological Society of America 101, 2308–2322. doi:10.1785/0120100076.

Dunham, E.M., Belanger, D., Cong, L., Kozdon, J.E., 2011b. Earthquake Ruptures with Strongly Rate-Weakening Friction and Off-Fault Plasticity, Part 1: Planar Faults. Bulletin of the Seismological Society of America 101, 2296–2307. URL: https://doi.org/10.1785/0120100075, doi:10.1785/0120100075.

Erickson, B.A., Jiang, J., Barall, M., Lapusta, N., Dunham, E.M., Harris, R., Abrahams, L.S., Allison, K.L., Ampuero, J., Barbot, S., Cattania, C., Elbanna, A., Fialko, Y., Idini, B., Kozdon, J.E., Lambert, V., Liu, Y., Luo, Y., Ma, X., Best McKay, M., Segall, P., Shi, P., van den Ende, M., Wei, M., 2020. The Community Code Verification Exercise for Simulating Sequences of Earthquakes and Aseismic Slip (SEAS). Seismological Research Letters doi:10.1785/0220190248.

Fang, Z., Dunham, E.M., 2013. Additional shear resistance from fault roughness and stress levels on geometrically complex faults. Journal of Geophysical Research: Solid Earth 118, 3642–3654. doi:10.1002/jgrb.50262.

Galetzka, J., Melgar, D., Genrich, J.F., Geng, J., Owen, S., Lindsey, E.O., Xu, X., Bock, Y., Avouac, J.P., Adhikari, L.B., Upreti, B.N., Pratt-Sitaula, B., Bhattarai, T.N., Sitaula, B.P., Moore, A., Hudnut, K.W., Szeliga, W., Normandeau, J., Fend, M., Flouzat, M., Bollinger, L., Shrestha, P., Koirala, B., Gautam, U., Bhatterai, M., Gupta, R., Kandel, T., Timsina, C., Sapkota, S.N., Rajaure, S., Maharjan, N., 2015. Slip pulse and resonance of the kathmandu basin during the 2015 gorkha earthquake, nepal. Science 349, 1091–1095. doi:10.1126/science.aac6383.

Heimisson, E.R., Dunham, E.M., Almquist, M., 2019. Poroelastic effects destabilize mildly rate-strengthening friction to generate stable slow slip pulses. Journal of the Mechanics and Physics of Solids 130, 262 – 279. doi:https://doi.org/10.1016/j.jmps.2019.06.007.

Kagan, Y.Y., 2002. Seismic moment distribution revisited: I. Statistical results. Geophysical Journal International 148, 520–541. doi:10.1046/j.1365-246x.2002.01594.x.

Lapusta, N., Liu, Y., 2009. Three-dimensional boundary integral modeling of spontaneous earthquake sequences and aseismic slip. Journal of Geophysical Research: Solid Earth 114. doi:10.1029/2008JB005934.

Lapusta, N., Rice, J.R., Ben-Zion, Y., Zheng, G., 2000. Elastodynamic analysis for slow tectonic loading with spontaneous rupture episodes on faults with rate- and state-dependent friction. Journal of Geophysical Research: Solid Earth 105, 23765–23789. doi:10.1029/2000JB900250.

Ma, X., Elbanna, A., 2019. Dynamic rupture propagation on fault planes with explicit representation of short branches. Earth and Planetary Science Letters 523, 115702. doi:https://doi.org/10.1016/j.epsl.2019.07.005.

Nikkhoo, M., Walter, T.R., Lundgren, P.R., Prats-Iraola, P., 2016. Compound dislocation models (cdms) for volcano deformation analyses. Geophysical Journal International , ggw427.

Ozawa, S.W., Hatano, T., Kame, N., 2019. Longer migration and spontaneous decay of aseismic slip pulse caused by fault roughness. Geophysical Research Letters 46, 636–643. doi:10.1029/2018GL081465.

Power, W.L., Tullis, T.E., 1991. Euclidean and fractal models for the description of rock surface roughness. Journal of Geophysical Research: Solid Earth 96, 415–424. doi:10.1029/90JB02107.

Power, W.L., Tullis, T.E., Brown, S.R., Boitnott, G.N., Scholz, C.H., 1987. Roughness of natural fault surfaces. Geophysical Research Letters 14, 29–32. doi:10.1029/GL014i001p00029.

Rice, J.R., 1993. Spatio-temporal complexity of slip on a fault. Journal of Geophysical Research: Solid Earth 98, 9885–9907. doi:10.1029/93JB00191.

Rice, J.R., Lapusta, N., Ranjith, K., 2001. Rate and state dependent friction and the stability of sliding between elastically deformable solids. J. Mech. Phys. Solids 49, 1865–1898.

Richards-Dinger, K., Dieterich, J.H., 2012. Rsqsim earthquake simulator. Seismological Research Letters 83, 983–990.

Rubin, A.M., Ampuero, J.P., 2005. Earthquake nucleation on (aging) rate and state faults. Journal of Geophysical Research: Solid Earth 110. doi:10.1029/2005JB003686.

Ruina, A., 1983. Slip instability and state variable friction laws. Journal of Geophysical Research: Solid Earth 88, 10359–10370. doi:10.1029/JB088iB12p10359.

Sagy, A., Brodsky, E.E., Axen, G.J., 2007. Evolution of fault-surface roughness with slip. Geology 35, 283–286. doi:10.1130/G23235A.1.

Shi, Z., Day, S.M., 2013. Rupture dynamics and ground motion from 3-d rough-fault simulations. Journal

of Geophysical Research: Solid Earth 118, 1122–1141. doi:10.1002/jgrb.50094.
Tal, Y., Hager, B.H., 2018a. Dynamic mortar finite element method for modeling of shear rupture on frictional rough surfaces. Computational Mechanics 61, 699–716.
Tal, Y., Hager, B.H., 2018b. The slip behavior and source parameters for spontaneous slip events on rough faults subjected to slow tectonic loading. Journal of Geophysical Research: Solid Earth 123, 1810–1823. doi:10.1002/2017JB014737.
Tal, Y., Hager, B.H., Ampuero, J.P., 2018. The effects of fault roughness on the earthquake nucleation process. Journal of Geophysical Research: Solid Earth 123, 437–456. doi:10.1002/2017JB014746.
Zheng, G., Rice, J.R., 1998. Conditions under which velocity-weakening friction allows a self-healing versus a cracklike mode of rupture. Bulletin of the Seismological Society of America 88, 1466–1483.